


Revealing the $\chi_{\text{eff}}-q$ correlation among Coalescing Binary Black Holes and Tentative Evidence for AGN-driven Hierarchical Mergers

YIN-JIE LI * (李银杰) ¹, YUAN-ZHU WANG * (王远瞩) ², SHAO-PENG TANG (唐少鹏) ¹, TONG CHEN (陈彤)³, AND
YI-ZHONG FAN (范一中) ^{1,4}

¹Key Laboratory of Dark Matter and Space Astronomy, Purple Mountain Observatory, Chinese Academy of Sciences, Nanjing 210023, People's Republic of China

²Institute for Theoretical Physics and Cosmology, Zhejiang University of Technology, Hangzhou, 310032, People's Republic of China

³School of Physical Science and Technology, Inner Mongolia University, Hohhot 010021, People's Republic of China

⁴School of Astronomy and Space Science, University of Science and Technology of China, Hefei, Anhui 230026, People's Republic of China

ABSTRACT

The origin of the correlation between the effective spins (χ_{eff}) and mass ratios (q) of LIGO-Virgo-KAGRA's binary black holes (BBHs) is still an open question. Motivated by the recent identification of two subpopulations of the BBHs, in this work we investigate the potential $\chi_{\text{eff}} - q$ correlation for each subpopulation. Surprisingly, the $\chi_{\text{eff}}-q$ correlation either significantly weakens or disappears for the low-mass subpopulation if we introduce a second χ_{eff} distribution for the high-mass subpopulation, which likely originates from hierarchical mergers. This suggests that the $\chi_{\text{eff}}-q$ correlation in the overall population can be explained by the superposition of two distinct subpopulations. We find Bayesian evidence strongly favoring two separate χ_{eff} distributions over a single mass-ratio-dependent distribution, with Bayes factors $\ln \mathcal{B} > 4.2$. The first subpopulation has a narrow χ_{eff} distribution peaking at ~ 0.05 , whose primary-mass function showing a rapid decline beyond $\sim 40M_{\odot}$, in agreement with first-generation BBHs. The second χ_{eff} distribution is broad and peaks at $\mu_{\chi,2} \sim 0.4$, aligning with predictions for hierarchical mergers in active galactic nucleus (AGN) disks. However, we cannot exclude negative χ_{eff} values in the second subpopulation, suggesting hierarchical mergers might occur both in AGN disks and stellar clusters. Furthermore, the inferred second χ_{eff} distribution might alternatively arise from other formation channels, such as stable mass transfer or chemically homogeneous evolution, if not interpreted as hierarchical mergers.

Keywords: Binary Black Holes; Gravitational Waves; Stellar Evolution; Active Galactic Nuclei

1. INTRODUCTION

The coalescing binary black holes (BBHs) will provide clues about their formation and evolutionary processes through the parameters of these systems (Mandel & Farmer 2022). In addition to characterizing the marginalized distributions of these parameters, it is also important to investigate the correlations among them (Heinzel et al. 2024; Callister 2024), including mass versus spin (e.g. Tiwari & Fairhurst 2021; Wang et al. 2022;

Li et al. 2024b,a), mass versus mass ratio (Li et al. 2022), spin versus mass ratio (Callister et al. 2021), redshift versus spin (Biscoveanu et al. 2022), and redshift versus mass versus spin (Tiwari 2022; Guo et al. 2024).

Callister et al. (2021), for the first time, reported the anti-correlation between the effective spins (χ_{eff}) and mass ratios (q) of BBHs with data from GWTC-2 (Abbott et al. 2019, 2021a). This anti-correlation was subsequently confirmed by Abbott et al. (2023a); Adamcewicz et al. (2023) with data from GWTC-3 (Abbott et al. 2019, 2021a, 2024, 2023b), though the evidence is reduced with a more flexible model (Heinzel et al. 2024). However, the origin of this anti-correlation is still in debate (Callister et al. 2021; Abbott et al. 2023a).

* Contributed equally.

The corresponding author: yzfan@pmo.ac.cn (Y.Z.F)

Many simulations suggested that hierarchical mergers in the disks of active galactic nucleus (AGNs) could explain the observed $\chi_{\text{eff}}-q$ correlation (e.g., McKernan et al. 2022; Santini et al. 2023; Cook et al. 2024). The spin orientations and orbital angular momenta of binary black holes (BBHs) will be modulated by the disks, causing the mergers to favor positive effective spins. Additionally, the migration traps in AGN disks will produce mergers involving multiple generations of black holes (BHs) that have unequal masses and larger (positive) effective spins. Previously, we found that the coalescing BHs can be divided into two subpopulations with significantly different spin-magnitude versus component-mass distributions, which are nicely consistent with first- and higher-generation BHs (Li et al. 2024b). We also found that a fraction of the population that we interpreted as hierarchical mergers have aligned spin tilts and asymmetric mass ratios, which may give rise to the $\chi_{\text{eff}}-q$ anti-correlation.

However, other simulations suggested that certain formation channels of isolated binaries can produce highly spinning and unequal-mass BBHs, particularly the stable mass transfer formation scenario (Banerjee & Olejak 2024). Because the progenitors of unequal BBH systems in the stable mass transfer formation scenario are more likely to efficiently shrink their orbits during the second Roche-lobe overflow, which makes them easier to enter the tidal spin-up regime and later merge due to GW emission (Olejak et al. 2024). Therefore, it is possible that there may be a correlation between the effective spin and mass ratio in first-generation (or low-spin) BBHs, or among potential isolated evolution channels (Wang et al. 2022; Godfrey et al. 2023; Li et al. 2024a).

In this study, we delve into the question of whether the anti-correlation between $\chi_{\text{eff}}-q$ in BBHs originates from a superposition of various formation channels / subpopulations (Li et al. 2024b), if it emerges from the evolutionary processes of a single population with a common formation channel (e.g., Banerjee & Olejak 2024), or alternatively, both effects have contributed to the observed correlation. Additionally, we investigate the χ_{eff} distribution in the high-mass range that might corresponds to the hierarchical mergers, in order to find out whether these events originate from the AGN disks, or alternatively from the star clusters which exhibits a symmetric χ_{eff} distribution (Payne et al. 2024; Antonini et al. 2025).

This work is organized as follows: In Section 2 and Section 3, we introduce the methods and the results. In Section 4, we present the conclusions and engage in discussions.

2. METHODS

We use hierarchical Bayesian inference to measure the hyperparameters of population model; see Appendix A for details. Following Abbott et al. (2023a), we adopted 69 BBH events with false alarm rates (FAR) $< 1\text{yr}^{-1}$ in GWTC-3 for analysis. The posterior samples for each BBH event are obtained from `events-zenodo`, and the ‘C01:Mixed’ samples are adopted.

We first use the same $\chi_{\text{eff}} - q$ distribution model as that used in Callister et al. (2021) to fit data of GWTC-3 for comparison. Specifically, the mean and width of the χ_{eff} distribution change linearly with q (referred to as the Base model); see Appendix B.2 for the detailed formula. The rate evolution model is the MD model (Madau & Dickinson 2014), as defined in the Appendix B.3. We use both the non-/semi-parametric formula POWERLAW+SPLINE (PS; Edelman et al. 2022; Abbott et al. 2023a) and the popular parametric formula POWERLAW+PEAK (PP; Talbot & Thrane 2018; Abbott et al. 2021b) to model the primary-mass distribution, see Appendix B.1 for the details of mass functions. With the PP model, we find an anti-correlation between χ_{eff} and q distribution (i.e., $a < 0$) at 99.2% credible level. However, the credibility decreases to 93% with the more flexible PS model, while the overall tendency remains unchanged, as shown in Figure 1.

Inspired by the investigation of spin-magnitude versus component-mass distribution (Li et al. 2024b), we introduce another χ_{eff} -distribution to capture the secondary subpopulation of BBHs that is consistent with hierarchical mergers. Two kind of models are applied, one is the Mixture model on primary-mass versus effective-spin distribution,

$$\pi_{\text{mix}}(m_1, m_2, \chi_{\text{eff}} | \mathbf{\Lambda}) = P(m_2 | m_1; \mathbf{\Lambda}) [\pi_1(m_1, \chi_{\text{eff}} | \mathbf{\Lambda})(1 - r_2) + \pi_2(m_1, \chi_{\text{eff}} | \mathbf{\Lambda})r_2], \quad (1)$$

with

$$\pi_1(m_1, \chi_{\text{eff}} | \mathbf{\Lambda}) = P_{1,m_1}(m_1 | \mathbf{\Lambda}) P(\chi_{\text{eff}} | q; \mu_{\chi,0}, \sigma_{\chi,0}, a, b) \quad (2)$$

and

$$\pi_2(m_1, \chi_{\text{eff}} | \mathbf{\Lambda}) = \mathcal{PL}(m_1 | -\alpha_2, m_{\text{min},2}, m_{\text{max},2}) \mathcal{G}_{[-1,1]}(\chi_{\text{eff}} | \mu_{\chi,2}, \sigma_{\chi,2}) \quad (3)$$

where r_2 is the mixed fraction of the second subpopulation, and $\mathcal{G}_{[-1,1]}$ is the truncated Gaussian distribution. P_{m_1} and \mathcal{PL} are the primary-mass functions for the two subpopulation, and we adopt \mathcal{PS} and \mathcal{PP} for P_{m_1} , respectively. $P(m_2 | m_1; \mathbf{\Lambda})$ is the normalized secondary-mass distribution conditioned on m_1 , $P(\chi_{\text{eff}} | q; \mu_{\chi,0}, \sigma_{\chi,0}, a, b)$ is the Base model that encodes

the $\chi_{\text{eff}} - q$ correlation (Callister et al. 2021), see Appendix B for the detailed formulas of the models. Note that we do not apply either the low-mass tapering function or the perturbation function to the power-law mass function for the second subpopulation, to avoid overly complex (bloated) models. Actually, with currently available data, the results are rather similar when the low-mass tapering and perturbation functions are applied, see Appendix C.

The other model has a more concise formula, i.e., the two χ_{eff} -distributions are modulated by a transition function of the primary mass (see also Wang et al. 2022; Li et al. 2024b; Guo et al. 2024, for similar constructions), hereafter Transition model,

$$\pi_{\text{tran}}(m_1, m_2, \chi_{\text{eff}} | \Lambda) = P_{m_1}(m_1 | \Lambda) P(m_2 | m_1; \Lambda) \quad (4)$$

$$P_{\text{tran}}(\chi_{\text{eff}} | q, m_1; \Lambda),$$

with

$$P_{\text{tran}}(\chi_{\text{eff}} | q, m_1; \Lambda) =$$

$$P(\chi_{\text{eff}} | q; \mu_{\chi,0}, \sigma_{\chi,0}, a, b) \frac{1}{1 + e^{(m_1 - m_t)/\delta_t}} +$$

$$\mathcal{G}_{[-1,1]}(\chi_{\text{eff}} | \mu_{\chi,2}, \sigma_{\chi,2}) \frac{1}{1 + e^{(m_t - m_1)/\delta_t}}, \quad (5)$$

where m_t and δ_t are the location and rapidness of the transition. For the BBHs with primary mass below / above m_t , the χ_{eff} distribution is dominated by the Base model / second Gaussian distribution.

3. RESULTS

In Table 1, we summarize the Bayes factors of the novel models in this work compared to the Base (PS) and Base (PP) models, respectively. For both PS and PP cases, the Transition model and Mixture model are favored than the Base models. Furthermore, the Transition model and Mixture model without the $\chi_{\text{eff}}-q$ correlation (i.e., $a = 0, b = 0$) are even more favored, with $\ln \mathcal{B} > 4.2$. Figure 1(right panels) shows the posteriors of the hyperparameters describing the χ_{eff} and q correlation. In each case, the parameters of the Transition model and Mixture model are highly consistent with each other. For the PS case, the slope parameters a and b are consistent with zero. For the PP case, the $\chi_{\text{eff}}-q$ correlation still remains, but the credibility of $a < 0$ decreases to $\sim 90\%$ comparing to the Base (PP) model. It is consistent in both cases that the anti-correlation reduces when we introduce a second subpopulation of χ_{eff} distribution, which means that the second subpopulation has contributed to the $\chi_{\text{eff}}-q$ correlation in the whole population. Specifically, the anti-correlation of the entire BBH population mainly results from the superposition of two subpopulations. However, whether

there is $\chi_{\text{eff}}-q$ correlation in the first subpopulation remains uncertain. Additionally, we find there is no evidence for the $\chi_{\text{eff}}-q$ correlation in the second subpopulation with currently available data, see Appendix D.2. In subsequent analysis, we adopt the results inferred with $a = 0, b = 0$, since the posterior distributions of parameters are broadly consistent with the results inferred with variable a and b , see Appendix C.

Table 1. Model comparison

Model	$\ln \mathcal{B}_{\text{PS}}^X$
Base(PS)	0
Base(PS) with $a = 0, b = 0$	0
Transition(PS)	4.9
Transition(PS) with $a = 0, b = 0$	6.7
Mixture(PS)	3.8
Mixture(PS) with $a = 0, b = 0$	6.1
Base(PP)	-5.9
	$\ln \mathcal{B}_{\text{PP}}^X$
Base(PP)	0
Base(PP) with $a = 0, b = 0$	-1.2
Transition(PP)	3.2
Transition(PP) with $a = 0, b = 0$	4.9
Mixture(PP)	2.7
Mixture(PP) with $a = 0, b = 0$	4.2

Note: All the log Bayes factors in the top / bottom are relative to the Base (PS) / (PP) model that encode the $\chi_{\text{eff}}-q$ correlation and accompanied with the PS / PP mass function.

We find that the second subpopulation shows a significantly different χ_{eff} distribution compared to the first subpopulation, see Figure 2. The divergence point of the Transition model in the primary-mass function is $m_t = 49_{-9}^{+13} M_\odot$ ¹, with a transition scale of $\delta_t = 6_{-4}^{+3} M_\odot$ ($\delta_t = 6_{-4}^{+4} M_\odot$) for the PS (PP) case. Note that m_t and δ_t are degenerated with each other, and δ_t is only loosely constrained, see Figure 3.

As for the Mixture model, though the maximum mass of the first subpopulation is not well constrained, the masses of 99.5th and 99.75th, and 99.9th percentiles are better measured. Specifically, the $m_{99.9\%}$ of the first subpopulation is significantly different from that of the entire population, see Appendix C. The minimum mass of the second subpopulation is $\sim 30 M_\odot$. These results are consistent with our previous analysis using spin mag-

¹ In this work, when quoting X_{-Z}^{+Y} , X means the posterior median and $[X - Y, Y + Z]$ means the central 90% credible interval.

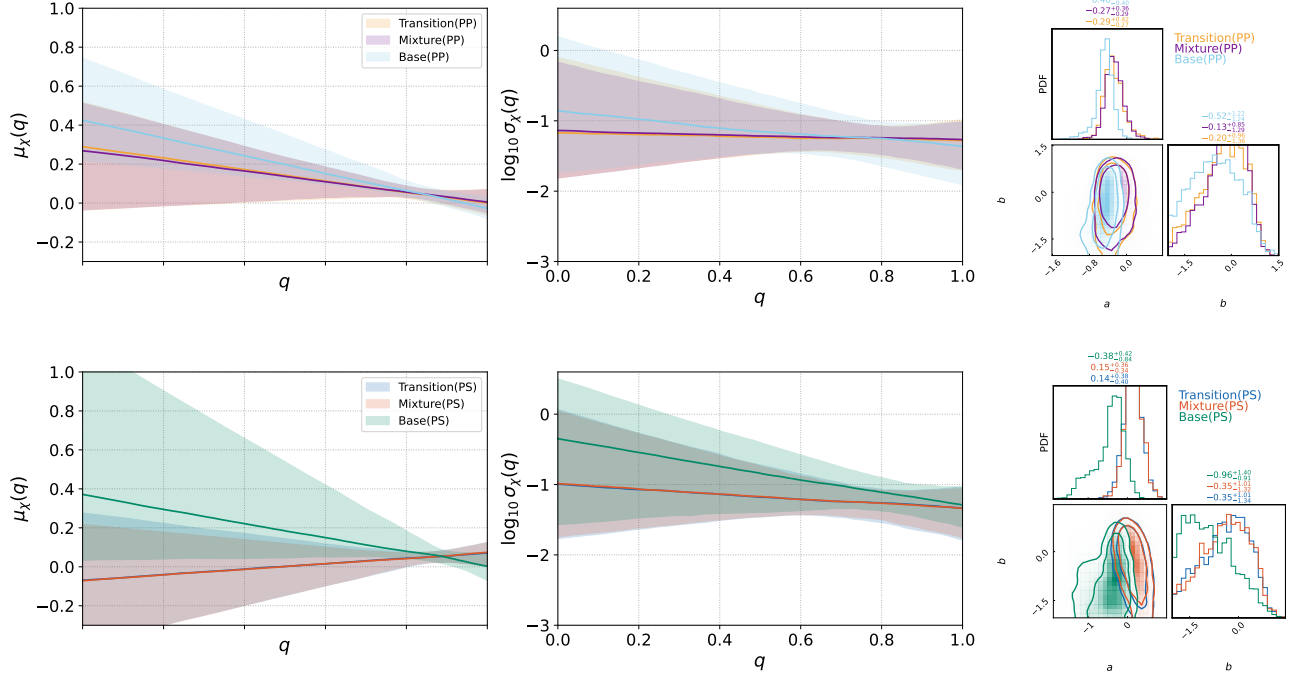


Figure 1. Left&Mid: Constraints on the mean $\mu_\chi(q)$ and standard deviation $\sigma_\chi(q)$ of the χ_{eff} distribution, as a function of BBH mass ratio q . The solid curves are the medians and the colored bands are the 90% credible intervals. Right: Posteriors of the hyperparameters describing the $\chi_{\text{eff}} - q$ correlation. The contours mark the central 50% and 90% posterior credible regions, the values represent the median and 90% credible intervals.

nitudes of BBHs (Wang et al. 2022; Li et al. 2024b), see Appendix C for the distributions of other related parameters. The χ_{eff} distributions of both subpopulations are not symmetric with respect to zero, indicating the presence of formation channels other than star clusters.

We find that $\mu_{\chi,2} > 0$ at 98% (95%) credible level, and a symmetric χ_{eff} distribution with respect to zero for the second population (i.e., $\mu_{\chi,2} = 0$) is disfavored by a Bayes factor of $\ln \mathcal{B} = 1.4$ ($\ln \mathcal{B} = 1.5$) for the PS (PP) case, which indicates that the hierarchical mergers cannot be produced (solely) by star clusters. The second χ_{eff} distribution is broad and peaks at $\mu_{\text{eff},2} = 0.40^{+0.32}_{-0.30}$ ($\mu_{\text{eff},2} = 0.39^{+0.39}_{-0.37}$) for the PS (PP) case, which is consistent with the hierarchical mergers in the AGN disks (Yang et al. 2019). However, some other formation channels, like chemically homogeneous evolution (Mandel & de Mink 2016) and stable mass transfer (Bavera et al. 2021) can not be ruled out based solely on the effective spin distribution (Zevin et al. 2021). We have also inferred using two more flexible model for the second χ_{eff} distribution, one with variable edges for the truncated Gaussian, the other is spline function (Golomb & Talbot 2023), see Appendix D.1. We find that the second χ_{eff} distribution is not symmetric about zero, but having preference for positive values. Additionally, the

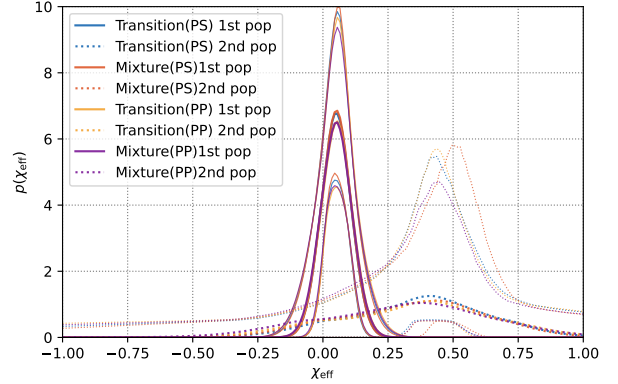


Figure 2. Effective-spin distributions of the two subpopulation inferred by the Transition and Mixture models with $a = 0, b = 0$. The lines represent the mean values and 90% credible intervals.

negative values for the second χ_{eff} distributions can not be ruled out.

4. CONCLUSIONS AND DISCUSSION

In this work, we investigate the origins of $\chi_{\text{eff}} - q$ correlation in the BBHs (Callister et al. 2021; Abbott et al. 2023a) with data of GWTC-3, using the dedicated models that introduce a second χ_{eff} distribution for the second (high-spin) subpopulation.

In both PS and PP cases, the $\chi_{\text{eff}}-q$ correlation significantly reduces when we include a second subpopulation for the χ_{eff} distribution. Additionally, there is no evidence for a $\chi_{\text{eff}} - q$ correlation in the second subpopulation, see Appendix D.2. Therefore we can conclude that the $\chi_{\text{eff}}-q$ anti-correlation of the entire BBH population mainly results from *the superposition of two subpopulations*. However, whether there is $\chi_{\text{eff}}-q$ correlation in the first subpopulation remains uncertain. Because for the PS case, a is consistent with zero, while for the PP case, we still find $a < 0$ at $\sim 90\%$ credible level, see Figure 1.

The stable mass transfer formation channel is expected to produce BBHs with $\chi_{\text{eff}} - q$ anti-correlation (Olejak et al. 2024; Banerjee & Olejak 2024), while BBHs from the common envelop channel may exhibit an opposite correlation (Bavera et al. 2020, 2021). Therefore, it is possible that there is a $\chi_{\text{eff}}-q$ correlation in the first subpopulation, which is consistent with the first-generation BBHs. Note that the first subpopulation may consist not only the isolated formation channels but also the dynamical formation channels (Ray et al. 2024; Li et al. 2024a). When the detections are enriched, more subpopulations may be recognized and the correlations of their parameters may also be measured.

The χ_{eff} distribution of the second subpopulation (shown in Figure 2), is consistent with the hierarchical mergers in gas-rich environments, such as AGN disks (Yang et al. 2019). Some other formation channels may also produce χ_{eff} distributions similar to that of the second subpopulation inferred with our models (see Zevin et al. 2021), such as chemically homogeneous evolution (Mandel & de Mink 2016) and stable mass transfer (Bavera et al. 2021). However, the second subpopulation found in this work is actually consistent with the population of hierarchical mergers found in our previous works (Li et al. 2024b), where we have provided smoking-gun evidence, specifically a spin-magnitude distribution of approximately 0.7 (Gerosa & Fishbach 2021). Therefore, hereafter we simply interpolate the second subpopulation as hierarchical mergers. Antonini et al. (2025) attributed this subpopulation to hierarchical mergers in star clusters, as they found that the χ_{eff} distribution is consistent with a uniform distribution in the range of approximately (-0.5, 0.5). To check out whether such difference is caused by the systematic bias in our analysis, we perform end-to-end mock data studies including the parameter estimation and hierarchical analysis of mock signals, see Appendix E. We find that the two subpopulations in the χ_{eff} distribution can be successfully recognized. Additionally, we repeat the simulation for many times, the recoveries of the second χ_{eff} distributions are always broadly consistent with the injections.

When injected distribution is symmetric (asymmetric), then the recovered distributions are almost symmetric (asymmetric). Thus, the identified asymmetry in the second subpopulation's χ_{eff} distribution in our study is attributed to the data itself rather than to methodological biases. With currently available data, we find the symmetric χ_{eff} distribution of the second subpopulation ($\mu_{\chi,2}$) is less favored by $\ln \mathcal{B} \sim 1.5$. A more conclusive evidence may be found when the data from the fourth observing run² are released.

Many simulations (e.g., Yang et al. 2019; Santini et al. 2023; Cook et al. 2024) show that the hierarchical mergers in disk-like environments can produce a χ_{eff} distribution peaking at ~ 0.4 that is consistent with our results. Additionally, AGN-driven mergers (including first generations) will exhibit a $\chi_{\text{eff}}-q$ correlation that is found in the entire BBH population (Santini et al. 2023; Cook et al. 2024). Therefore, it is very likely that AGN-disk channel has contributed to the BBHs detected by LVKC (Abbott et al. 2019, 2021a, 2024, 2023b). Some works also suggest that the BBHs with primary masses at $\sim 35M_{\odot}$ peak are consistent with dynamical formation channels in star clusters (Li et al. 2024a; Ray et al. 2024), as predicted by Antonini et al. (2023). Therefore, the star clusters have also contributed to the hierarchical mergers, if the remnants of the previous mergers are sufficiently retained in the environments (Gerosa & Fishbach 2021; Zevin & Holz 2022; Li & Fan 2024). Our further analysis with a more flexible models also show that the negative values for the second χ_{eff} distributions can not be ruled out, see Appendix D.1.

However, there are only ~ 11 hierarchical mergers (high-spin events) in GWTC-3 (Li et al. 2024b), making it difficult to determine the mixture fractions of AGN-disk like and star-cluster formation channels. We will address such issue when the GW data are significantly enriched. The fourth observing run (O4) of the LIGO-Virgo-KAGRA GW detectors is currently underway, and the number of detections is rapidly increasing (see <https://gracedb.ligo.org/latest/>). At the end of O4, more than four times as many events are expected to be observed compared to O3 (Callister 2024). With the enriched data more subpopulations / formation channels of BBHs may be identified (Zevin et al. 2021), and the mixture fractions and the parameter correlations of subpopulations can be better determined (Li et al. 2022, 2024a; Guo et al. 2024; Heinzl et al. 2024; Callister 2024).

² See <https://gracedb.ligo.org/superevents/public/O4/> for the catalog of detection candidates.

Software: Bilby (Ashton et al. 2019, version 1.1.4, ascl:1901.011, <https://git.ligo.org/lscsoft/bilby/>), PyMultiNest (Buchner 2016, version 2.11, ascl:1606.005, <https://github.com/JohannesBuchner/PyMultiNest>).

This work is supported by the National Natural Science Foundation of China (No. 12233011), the General Fund (No. 2024M753495) of the China Postdoctoral Science Foundation, and the Priority Research Program of the Chinese Academy of Sciences (No. XDB0550400). Y-Z Wang is supported by the National Natural Science Foundation of China (No. 12203101) and S-P Tang is supported by the National Natural Science Foundation of China (No. 12303056), the General Fund (No. 2023M733736) and the Postdoctoral Fellowship Program (GZB20230839) of the China Postdoctoral Science Foundation. This research has made use of data and software obtained from the Gravitational Wave Open Science Center (<https://www.gwopenscience.org>), a service of LIGO Laboratory, the LIGO Scientific Collaboration and the Virgo Collaboration. LIGO is funded by the U.S. National Science Foundation. Virgo is funded by the French Centre National de Recherche Scientifique (CNRS), the Italian Istituto Nazionale della Fisica Nucleare (INFN) and the Dutch Nikhef, with contributions by Polish and Hungarian institutes.

APPENDIX

A. HIERARCHICAL BAYESIAN INFERENCE

We perform hierarchical Bayesian inference to infer the hyperparameters Λ describing population models $\pi(\theta|\Lambda)$. Following the framework described in (Mandel et al. 2019; Abbott et al. 2021b, 2023a), given Λ , the likelihood of the GW data $\{d\}$ from N_{det} detections can be expressed as,

$$\mathcal{L}(\{d\}|\Lambda) \propto N^{N_{\text{det}}} e^{-N_{\text{exp}}} \prod_i^{N_{\text{det}}} \int \pi(\theta_i|\Lambda) \mathcal{L}(d_i|\theta_i) d\theta_i, \quad (\text{A1})$$

where N is the total number of mergers in the surveyed time-space volume, which is related to the merger rate density over cosmic history $N = \int R(z|\Lambda) \frac{dV_c}{dz} \frac{T_{\text{obs}}}{1+z} dz$. N_{exp} is the expected number of detections, which is related to the detection probability $P(\text{det}|\theta)$, i.e., $N_{\text{exp}} = N \int P(\text{det}|\theta) \pi(\theta|\Lambda) d\theta$. This term can be calculated using a Monte Carlo integral over the referred injection³, see Appendix of Abbott et al. (2021b) for details. $\mathcal{L}(d_i|\theta_i)$ is the likelihood of the i -th event, which can be evaluated using the posterior samples (see Abbott et al. 2021b, for detailed illustration).

Following Abbott et al. (2023a); Talbot & Golomb (2023), we define the effective number of samples for the i -th event in the Monte Carlo integral as $N_{\text{eff},i} = \frac{[\sum_j w_{i,j}]^2}{\sum_j w_{i,j}^2}$, where $w_{i,j}$ is the weight of j -th sample in i -th event. We constrain $N_{\text{eff},i} > 10$ to ensure accurate evaluation of likelihood, which is sufficiently high given the sample size of GWTC-3 (Essick & Farr 2022). Additionally, we constrain the effective number of found injections remaining after population reweighting as $N_{\text{eff,sel}} > 4N_{\text{det}}$, to ensure an accurate estimation of N_{exp} (Farr 2019; Abbott et al. 2021b).

³ Adopted from <https://zenodo.org/doi/10.5281/zenodo.5636815>.

B. POPULATION MODELS

B.1. *Mass function*

The parametric primary-mass function is the popular POWERLAW+PEAK model (Abbott et al. 2021b), which reads,

$$\begin{aligned} \mathcal{PP}(m_1|\mathbf{\Lambda}) &\propto \\ &[\mathcal{PL}(m_1|-\alpha, m_{\min}, m_{\max})(1-\lambda_{\text{peak}})+ \\ &\mathcal{G}_{[m_{\min}, m_{\max}]}(m_1|\mu_m, \sigma_m)\lambda_{\text{peak}}] \times \mathcal{S}(m_1|\delta_m, m_{\min}), \end{aligned} \quad (\text{B2})$$

where $\mathcal{PL}(m_1|-\alpha, m_{\min}, m_{\max})$ is the Power-law distribution with slope index of $-\alpha$ truncated on (m_{\min}, m_{\max}) . \mathcal{G} is the Gaussian distribution with mean μ_m and width σ_m truncated on (m_{\min}, m_{\max}) , $\mathcal{S}(m_1|\delta_m, m_{\min})$ is the smooth function with smooth scale of δ_m , impacting on the low edge m_{\min} .

In order to reduce the bias that may be brought by the mis-specification of parametric formulas, we use a semi-/non-parametric mass function (Edelman et al. 2022) for the main analysis,

$$\begin{aligned} \mathcal{PS}(m_1|\mathbf{\Lambda}) &\propto \mathcal{PL}(m_1|-\alpha, m_{\min}, m_{\max}) \\ &\times \mathcal{S}(m_1|\delta_m, m_{\min})e^{f(m|\{x_i\}, \{f_i\})}, \end{aligned} \quad (\text{B3})$$

where $f(m|\{x_i\}, \{f_i\})$ is the cubic-spline perturbation function interpolated between the knots (x_i, f_i) placed in the mass range. Here we adopted 12 knots $\{x_i\}_{i=0}^{12}$ linearly distributed in log space of $(6, 80)M_{\odot}$, and restrict the perturbation to zero at the minimum and maximum knots.

The secondary-mass function is conditioned on the primary mass (Abbott et al. 2021b),

$$P(m_2|m_1; \mathbf{\Lambda}) \propto \mathcal{PL}(m_2|\beta, m_{\min}, m_1)\mathcal{S}(m_2|\delta_m, m_{\min}). \quad (\text{B4})$$

B.2. *Effective-spin distribution model*

We follow Callister et al. (2021) to construct a mass-ratio-dependent model for effective-spin distribution, i.e., the Base model,

$$\begin{aligned} P(\chi_{\text{eff}}|q; \mu_{\chi,0}, \sigma_{\chi,0}, a, b) &= \\ \mathcal{G}_{[-1,1]}(\mu_{\chi}(q; \mu_{\chi,0}, a), \sigma_{\chi}(q; \sigma_{\chi,0}, b)), \end{aligned} \quad (\text{B5})$$

with

$$\begin{aligned} \mu_{\chi}(q; \mu_{\chi,0}, a) &= \mu_{\chi,0} + a(q - 0.5), \\ \log \sigma_{\chi}(q; \sigma_{\chi,0}, b) &= \log \sigma_{\chi,0} + b(q - 0.5), \end{aligned} \quad (\text{B6})$$

where $\mathcal{G}_{[-1,1]}$ is the Gaussian truncated on $[-1, 1]$. Note that the linear functions in Abbott et al. (2023a) is slightly different, where the authors let $\mu_{\chi}(q=1) = \mu_{\chi,0}$ and $\log \sigma_{\chi}(q=1) = \log \sigma_{\chi,0}$.

B.3. *Rate evolution model*

The merger rate density as a function of redshift reads (MD model Madau & Dickinson 2014),

$$R(z|\gamma, \kappa, z_p) = R_0 \times \frac{[(1+z_p)^{(\gamma+\kappa)} + 1](1+z)^{\gamma}}{(1+z)^{(\gamma+\kappa)} + (1+z_p)^{(\gamma+\kappa)}}, \quad (\text{B7})$$

where R_0 is the local merger rate density. Note the injection campaign only provides mock events with $z < 1.9$, so we normalize the redshift distribution $P(z|\gamma, \kappa, z_p)$ within $(0, 1.9)$, when calculating likelihood.

C. ADDITIONAL RESULTS

Figure 3 and Figure 4 present the full hyperparameters (except for the interpolation knots) of the Transition model, and Mixture model respectively. We find that whether we fix $a=0, b=0$ or not does not affect the transition / classification of the two subpopulations. These results are consistent with the analysis using spin-magnitude distributions in our previous work (Li et al. 2024b). We observe that the results of the two models are well consistent with each other. The first χ_{eff} distribution narrowly peaks at ~ 0.05 , while the second χ_{eff} distribution peaks at ~ 0.4 , favoring a contribution from hierarchical mergers in AGN disks (Yang et al. 2019). Note that some other formation channels,

Table 2. Summary of model parameters.

Parameter	Description	Prior
$m_{\min}[M_{\odot}]$	The minimum mass	$U(2, 10)$
$m_{\max}[M_{\odot}]$	The maximum mass	$U(30, 100)$
α	Slope index of the power-law mass function	$U(-8, 8)$
$\delta_{\text{m}}[M_{\odot}]$	Smooth scale of the mass lower edge	$U(0, 10)$
β_q	Slope index of the mass-ratio distribution	$U(-8, 8)$
Special for POWERLAW+PEAK		
λ_{peak}	Fraction in the Gaussian component	$U(0, 1)$
$\mu_{\text{m}}[M_{\odot}]$	Mean of the Gaussian component	$U(20, 50)$
$\sigma_{\text{m}}[M_{\odot}]$	Width of the Gaussian component	$U(1, 10)$
Special for POWERLAW+SPLINE		
$\{f_i\}_{i=2}^{11}$	Interpolation values of perturbation for mass function	$\mathcal{N}(0, 1)$
Effective-spin distribution model		
$\mu_{\chi,0}$	Mean of χ_{eff} distribution given $q = 0.5$	$U(-1, 1)$
$\lg \sigma_{\chi,0}$	Log width of χ_{eff} distribution given $q = 0.5$	$U(-1.5, 0.5)$
a	Correlation between μ_{χ} and q	$U(-2.5, 2.5)$
b	Correlation between $\log \sigma_{\chi}$ and q	$U(-2, 2)$
Rate evolution model		
$\lg(R_0[\text{Gpc}^{-3} \text{ yr}^{-1}])$	Local merger rate density	$U(-3, 3)$
z_p	Peak point for the rate evolution function	$U(0, 4)$
γ	Slope of the power-law regime before z_p	$U(-8, 8)$
κ	Slope of the power-law regime after z_p	$U(-8, 8)$
Transition model		
$m_{\text{t}}[M_{\odot}]$	The transition point in primary-mass function	$U(20, 70)$
$\delta_{\text{t}}[M_{\odot}]$	Smooth scale of the transition	$U(0, 10)$
$\mu_{\chi,2}$	Mean of χ_{eff} distribution for secondary subpopulation	$U(-1, 1)$
$\lg \sigma_{\chi,2}$	Log width of χ_{eff} distribution secondary subpopulation	$U(-1.5, 0.5)$
Mixture model		
$m_{\min,2}[M_{\odot}]$	Minimum mass of the secondary component	$U(10, 50)$
$m_{\max,2}[M_{\odot}]$	Maximum mass of the secondary component	$U(50, 100)$
α_2	Index of m_1 distribution in the secondary component	$U(-8, 8)$
$\mu_{\chi,2}$	Mean of χ_{eff} distribution for secondary subpopulation	$U(-1, 1)$
$\lg \sigma_{\chi,2}$	Log width of χ_{eff} distribution secondary subpopulation	$U(-1.5, 0.5)$
r_2	fraction of the secondary component	$U(0, 1)$

Note: U and \mathcal{N} are for Uniform and Normal distribution.

such as stable mass transfer (Bavera et al. 2021) and chemically homogeneous evolution (Mandel & de Mink 2016) can also produce the χ_{eff} distributions peaking at positive values.

For the Mixture models, the maximum mass of the first subpopulation is not well constrained but exhibits a tail extending to larger values, see Figure 4. However, the masses of 99.5th and 99.75th, and 99.9th percentiles for the first subpopulation are well measured. Especially the $m_{99\%}$ of the first subpopulation differs significantly from that of the entire population inferred from the base models, see Figure 5.

Figure 6 presents the mass distributions of the subpopulations and the entire population inferred with different models. A consistent feature across all models (Mixture and Transition) is the rapid decline of the first subpopulation's mass distribution above $\sim 40M_{\odot}$, aligning with the BH mass gap predicted by the Pair-instability Supernova (Farmer et al. 2019). The second subpopulation dominates the high-mass range; however, the lower boundary of its mass distribution remains uncertain. We additionally tested a more flexible mass function for the second subpopulation in the Mixture (PS) model by applying low-mass tapering and perturbation functions to the second power-law component

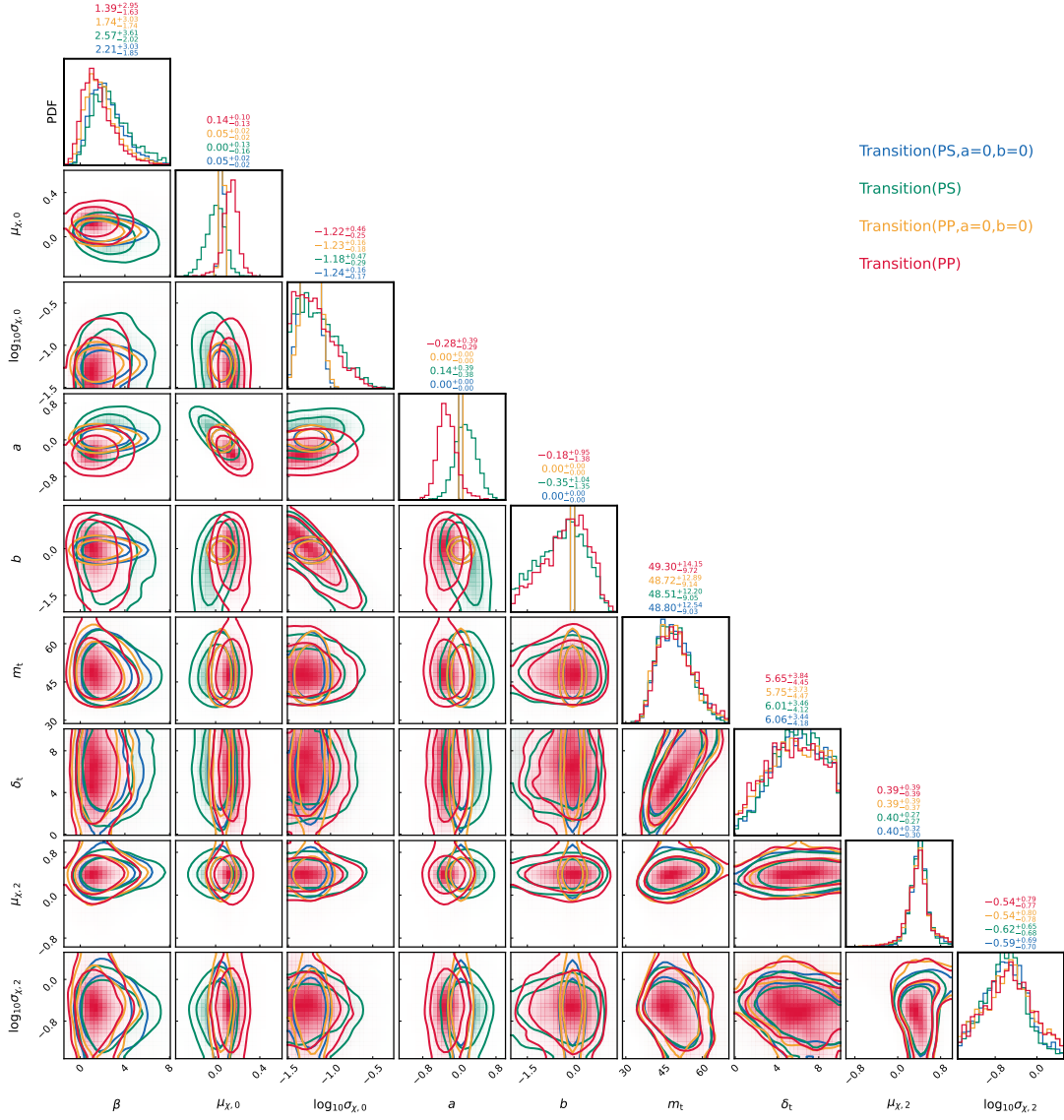


Figure 3. Posteriors of the special hyperparameters for the Transition model. The contours mark the central 50% and 90% posterior credible regions, the values represent the median and 90% credible intervals.

(labeled PS+PS). Despite this modification, the results are nearly identical to those without low-mass tapering and perturbation functions, as demonstrated in Figure 6.

D. THE SECOND SUBPOPULATION

D.1. Is the second χ_{eff} distribution symmetric?

The symmetry of χ_{eff} distribution is critical for determining the formation environments of hierarchical mergers. Hierarchical mergers in star clusters always exhibit a symmetric χ_{eff} distribution about zero (Payne et al. 2024; Fishbach et al. 2022). While AGN-driven hierarchical mergers tend to favor positive χ_{eff} due to gas torques (McKernan et al. 2018). In this section, we use two extended models to investigate the χ_{eff} distribution of the second subpopulation. The accompanied mass function is the PS model. First, we infer with variable lower edge and upper edge ($\chi_{\text{min},2}$, $\chi_{\text{max},2}$) for the second χ_{eff} distribution (labeled Truncated). We infer that $\chi_{\text{max},2} > 0.4$ at 97% credible level. However, the $\chi_{\text{min},2}$ is only poorly constrained. Second, we implement a spline-based model for the second χ_{eff} distribution (labeled Spline), $P_S(\chi_{\text{eff}}) \propto e^{f(\chi_{\text{eff}})}[-1, 1]$. $f(x)$ is a cubic spline function defined by 6 nodes linearly located in $[-1, 1]$. We

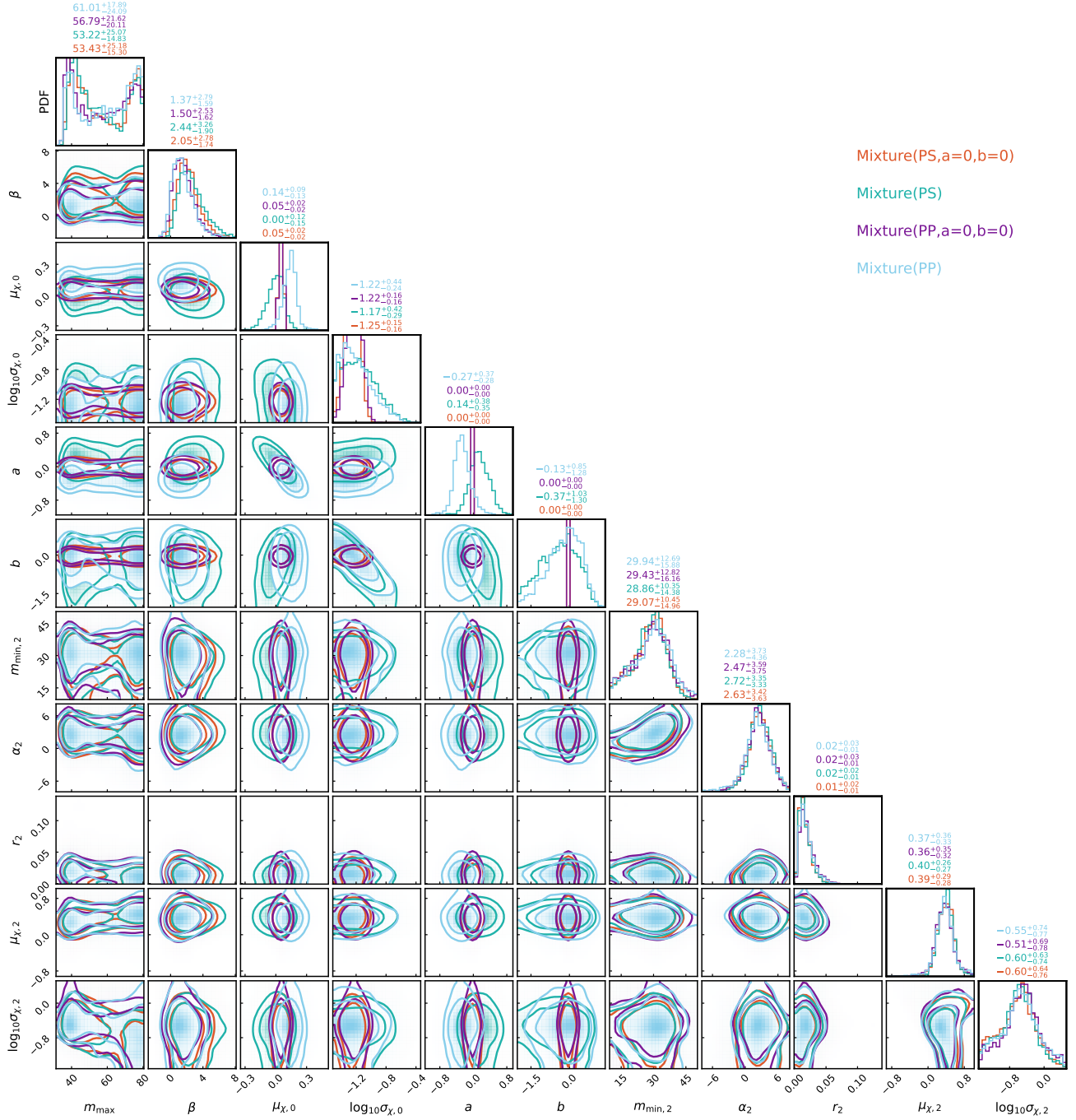


Figure 4. Posteriors of the special hyperparameters for the Mixture model. The contours mark the central 50% and 90% posterior credible regions, the values represent the median and 90% credible intervals.

restrict the 1-st and 6-th nodes to be -10 corresponding to $P_S(\chi_{\text{eff}} = 1)$, $P_S(\chi_{\text{eff}} = -1) \sim 0$, and the priors on the amplitude of 2-nd to 5-th nodes are unit Gaussian distributions (Golomb & Talbot 2023).

Figure 7 presents the χ_{eff} distributions inferred from the Truncated model and Spline model. The χ_{eff} distributions of the first subpopulation show high consistency between both models. For the second subpopulation, both models exhibit a preference for positive χ_{eff} values, though negative values cannot be ruled out based on the current constraints.

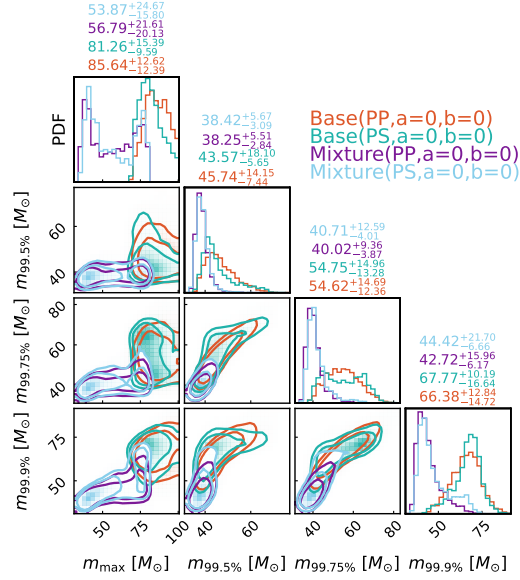


Figure 5. Posteriors of the maximum mass, masses of 99.5th and 99.75th, and 99.9th percentiles of the first subpopulation for the Mixture models. The contours mark the central 50% and 90% posterior credible regions, the values represent the median and 90% credible intervals.

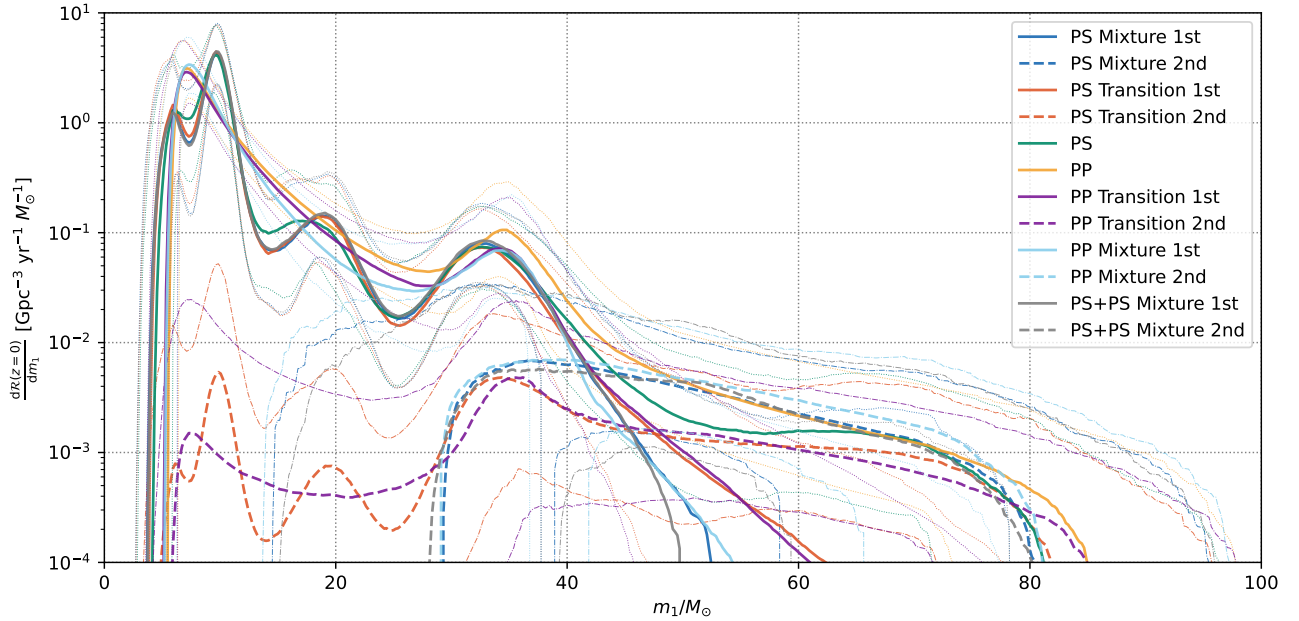


Figure 6. Mass distributions inferred with various models. The thick and thin lines represent the mean values and 90% credible intervals.

D.2. Is there $\chi_{\text{eff}} - q$ correlation in the second subpopulation?

To test whether there is $\chi_{\text{eff}} - q$ correlation in the second subpopulation, we extend the Transition model, i.e., replacing the second χ_{eff} distribution $\mathcal{G}_{[-1,1]}(\chi_{\text{eff}}|\mu_{\chi,2}, \sigma_{\chi,2})$ with $\mathcal{G}_{[-1,1]}(\mu_{\chi}(q; \mu_{\chi,2}, a_2), \sigma_{\chi}(q; \sigma_{\chi,2}, b_2))$. We find there is no evidence for the $\chi_{\text{eff}} - q$ correlation in the second subpopulation, as shown in Figure 8. Therefore, comparing the Base models and the Transition / Mixture models, we can conclude that the $\chi_{\text{eff}} - q$ anti-correlation in the entire population is mainly attributed to the superposition of two subpopulations.

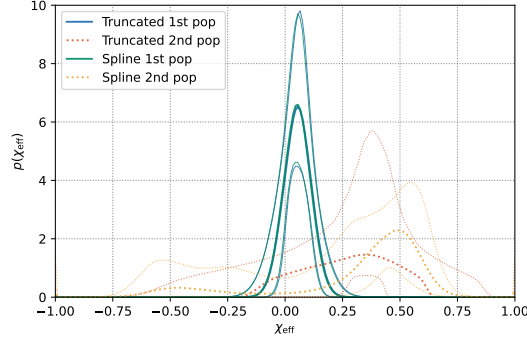


Figure 7. χ_{eff} distributions inferred using Transition (PS) with Truncated model and Spline model describing the second χ_{eff} distribution. The thick and thin lines represent the mean values and 90% credible intervals.

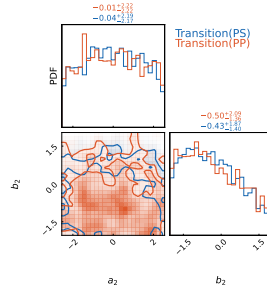


Figure 8. Hyperparameters describing the $\chi_{\text{eff}} - q$ correlation for the second subpopulation. The contours mark the central 50% and 90% posterior credible regions, the values represent the median and 90% credible intervals.

E. MOCK DATA STUDIES

To test the validity of our findings, we conduct an end-to-end injection study, including the parameter estimation and hierarchical analysis of mock signals. We generate three distinct mock populations. The first has a non-evolving χ_{eff} distribution (hereafter NonEvo). The second has the same feature that inferred with the Transition model in real data (hereafter TF&Asym). The third is similar to the second one, but for the χ_{eff} of high-mass BBHs exhibiting a symmetric distribution about zero (hereafter TF&Sym). Then we use the non-evolving model and Transition model to recover the features in the mock populations.

For all three mock populations, the mass distributions are generated by the PP model with $m_{\text{min}} = 5 M_{\odot}$, $m_{\text{max}} = 80 M_{\odot}$, $\delta_m = 5 M_{\odot}$, $\alpha = 3.5$, $\beta = 1$, $\mu_m = 35 M_{\odot}$, $\sigma_m = 3 M_{\odot}$, $\lambda_{\text{peak}} = 0.02$, the merger rate density as a function of redshift follows Eq. (B7) with $\gamma = 2.7$, $z_p = 2$, and $\kappa = 4$. For the NonEvo case, the χ_{eff} distribution follows a Gaussian distribution $\mathcal{G}_{[-1,1]}(\mu_{\chi}, \sigma_{\chi})$ with $\mu_{\chi} = 0.06$ and $\sigma_{\chi} = 0.1$. For the TF&Asym case, the χ_{eff} distribution exhibits mass dependence, i.e., the subpopulation with primary masses $< 40 M_{\odot}$ follows a Gaussian distribution $\mathcal{G}_{[-1,1]}(\mu_{\chi,1}, \sigma_{\chi,1})$ with $\mu_{\chi,1} = 0.05$ and $\sigma_{\chi,1} = 0.05$, and the subpopulation with primary masses $> 40 M_{\odot}$ follows a Gaussian distribution $\mathcal{G}_{[-1,1]}(\mu_{\chi,2}, \sigma_{\chi,2})$ with $\mu_{\chi,2} = 0.3$ and $\sigma_{\chi,2} = 0.3$. The TF&Sym case modifies the TF&Asym scenario by setting $\mu_{\chi,2} = 0$ while maintaining other parameters identical.

The mock detections are sampled from the injection campaign for O3 Search Sensitivity Estimates⁴ with the inverse FAR > 1 yr and the weight proportional to $p(\theta|\mathbf{\Lambda})/p_{\text{draw}}(\theta)$, where $p(\theta|\mathbf{\Lambda})$ is probability distribution of the mock population, and $p_{\text{draw}}(\theta)$ is the probability distribution from which the injection campaigns are drawn. For each case, we adopt 69 events. Following Callister et al. (2021), we set aligned spin components to $\chi_{1,z} = \chi_{2,z} = \chi_{\text{eff}}$ and in-plane components to zero. Then we use IMRPhenomXAS waveform (Pratten et al. 2020) to generate GW signal and inject it to the noise generated by the “O3 actual” noise power spectral densities⁵. We perform parameter estimation on each event using BILBY (Ashton et al. 2019), with the NESSAI nested sampler (Williams et al. 2025).

⁴ <https://doi.org/10.5281/zenodo.7890437>

⁵ <https://dcc.ligo.org/LIGO-T2000012/public>

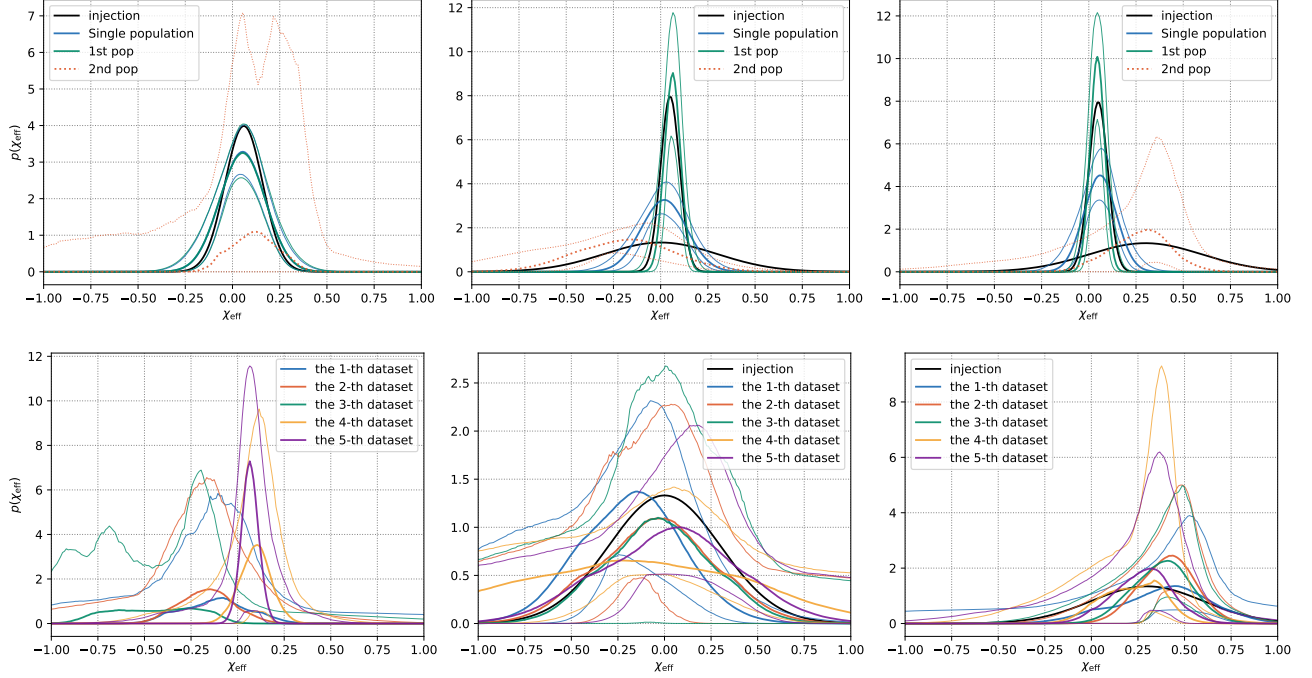


Figure 9. Top: χ_{eff} distributions recovered from mock population with Transition model and non-evolving model, the black lines are for the injections. Bottom: the χ_{eff} distributions of the second sub-population recovered from several datasets, the black lines are for the distribution of the second sub-populations. The thick and thin lines are for the mean values and 90% credible intervals.

For each case, we employ the non-evolution model and transition model to recover the mock population, i.e., Base (PP) with $a, b = 0$ and Transition (PP) with $a, b = 0$. The recovered χ_{eff} distributions are presented in Figure 9 (Top). It is shown that two distinct sub-populations are successfully recognized by the transition model in the TF&Sym and the TF&Asym mock populations. As anticipated, the second sub-population is ambiguous for the NonEvo mock population. For both the TF&Sym and the TF&Asym cases, the Transition model is more favored than the Base by $\ln \mathcal{B} \sim 8$. conversely, in the NonEvo case, the Transition model is less favored by $\ln \mathcal{B} \sim -1.5$.

To further assess the robustness of our analysis, we repeated the entire simulation process many times, including mock population generation, injection, recovery, and hierarchical inference. All runs produced consistent results, as illustrated in the bottom panel of Figure 9.

REFERENCES

- Abbott, B. P., Abbott, R., Abbott, T. D., et al. 2019, Physical Review X, 9, 031040, doi: [10.1103/PhysRevX.9.031040](https://doi.org/10.1103/PhysRevX.9.031040)
- Abbott, R., Abbott, T. D., Abraham, S., et al. 2021a, Physical Review X, 11, 021053, doi: [10.1103/PhysRevX.11.021053](https://doi.org/10.1103/PhysRevX.11.021053)
- . 2021b, ApJL, 913, L7, doi: [10.3847/2041-8213/abe949](https://doi.org/10.3847/2041-8213/abe949)
- Abbott, R., Abbott, T. D., Acernese, F., et al. 2023a, Physical Review X, 13, 011048, doi: [10.1103/PhysRevX.13.011048](https://doi.org/10.1103/PhysRevX.13.011048)
- . 2023b, Physical Review X, 13, 041039, doi: [10.1103/PhysRevX.13.041039](https://doi.org/10.1103/PhysRevX.13.041039)
- . 2024, PhRvD, 109, 022001, doi: [10.1103/PhysRevD.109.022001](https://doi.org/10.1103/PhysRevD.109.022001)
- Adamcewicz, C., Lasky, P. D., & Thrane, E. 2023, ApJ, 958, 13, doi: [10.3847/1538-4357/acf763](https://doi.org/10.3847/1538-4357/acf763)
- Antonini, F., Gieles, M., Dosopoulou, F., & Chattopadhyay, D. 2023, MNRAS, 522, 466, doi: [10.1093/mnras/stad972](https://doi.org/10.1093/mnras/stad972)
- Antonini, F., Romero-Shaw, I. M., & Callister, T. 2025, PhRvL, 134, 011401, doi: [10.1103/PhysRevLett.134.011401](https://doi.org/10.1103/PhysRevLett.134.011401)
- Ashton, G., Hübner, M., Lasky, P. D., et al. 2019, Bilby: Bayesian inference library, Astrophysics Source Code Library, record ascl:1901.011. <http://ascl.net/1901.011>

- Banerjee, S., & Olejak, A. 2024, arXiv e-prints, arXiv:2411.15112, doi: [10.48550/arXiv.2411.15112](https://doi.org/10.48550/arXiv.2411.15112)
- Bavera, S. S., Fragos, T., Qin, Y., et al. 2020, *A&A*, 635, A97, doi: [10.1051/0004-6361/201936204](https://doi.org/10.1051/0004-6361/201936204)
- Bavera, S. S., Fragos, T., Zevin, M., et al. 2021, *A&A*, 647, A153, doi: [10.1051/0004-6361/202039804](https://doi.org/10.1051/0004-6361/202039804)
- Biscoveanu, S., Callister, T. A., Haster, C.-J., et al. 2022, *ApJL*, 932, L19, doi: [10.3847/2041-8213/ac71a8](https://doi.org/10.3847/2041-8213/ac71a8)
- Buchner, J. 2016, PyMultiNest: Python interface for MultiNest, Astrophysics Source Code Library, record ascl:1606.005. <http://ascl.net/1606.005>
- Callister, T. A. 2024, arXiv e-prints, arXiv:2410.19145, doi: [10.48550/arXiv.2410.19145](https://doi.org/10.48550/arXiv.2410.19145)
- Callister, T. A., Haster, C.-J., Ng, K. K. Y., Vitale, S., & Farr, W. M. 2021, *ApJL*, 922, L5, doi: [10.3847/2041-8213/ac2ccc](https://doi.org/10.3847/2041-8213/ac2ccc)
- Cook, H. E., McKernan, B., Ford, K. E. S., et al. 2024, arXiv e-prints, arXiv:2411.10590, doi: [10.48550/arXiv.2411.10590](https://doi.org/10.48550/arXiv.2411.10590)
- Edelman, B., Doctor, Z., Godfrey, J., & Farr, B. 2022, *ApJ*, 924, 101, doi: [10.3847/1538-4357/ac3667](https://doi.org/10.3847/1538-4357/ac3667)
- Essick, R., & Farr, W. 2022, arXiv e-prints, arXiv:2204.00461, doi: [10.48550/arXiv.2204.00461](https://doi.org/10.48550/arXiv.2204.00461)
- Farmer, R., Renzo, M., de Mink, S. E., Marchant, P., & Justham, S. 2019, *ApJ*, 887, 53, doi: [10.3847/1538-4357/ab518b](https://doi.org/10.3847/1538-4357/ab518b)
- Farr, W. M. 2019, *Research Notes of the American Astronomical Society*, 3, 66, doi: [10.3847/2515-5172/ab1d5f](https://doi.org/10.3847/2515-5172/ab1d5f)
- Fishbach, M., Kimball, C., & Kalogera, V. 2022, *ApJL*, 935, L26, doi: [10.3847/2041-8213/ac86c4](https://doi.org/10.3847/2041-8213/ac86c4)
- Gerosa, D., & Fishbach, M. 2021, *Nature Astronomy*, 5, 749, doi: [10.1038/s41550-021-01398-w](https://doi.org/10.1038/s41550-021-01398-w)
- Godfrey, J., Edelman, B., & Farr, B. 2023, arXiv e-prints, arXiv:2304.01288, doi: [10.48550/arXiv.2304.01288](https://doi.org/10.48550/arXiv.2304.01288)
- Golomb, J., & Talbot, C. 2023, *PhRvD*, 108, 103009, doi: [10.1103/PhysRevD.108.103009](https://doi.org/10.1103/PhysRevD.108.103009)
- Guo, W.-H., Li, Y.-J., Wang, Y.-Z., et al. 2024, *ApJ*, 975, 54, doi: [10.3847/1538-4357/ad758a](https://doi.org/10.3847/1538-4357/ad758a)
- Heinzel, J., Vitale, S., & Biscoveanu, S. 2024, *PhRvD*, 109, 103006, doi: [10.1103/PhysRevD.109.103006](https://doi.org/10.1103/PhysRevD.109.103006)
- Li, G.-P., & Fan, X.-L. 2024, arXiv e-prints, arXiv:2411.09195, doi: [10.48550/arXiv.2411.09195](https://doi.org/10.48550/arXiv.2411.09195)
- Li, Y.-J., Tang, S.-P., Gao, S.-J., Wu, D.-C., & Wang, Y.-Z. 2024a, *ApJ*, 977, 67, doi: [10.3847/1538-4357/ad83b5](https://doi.org/10.3847/1538-4357/ad83b5)
- Li, Y.-J., Wang, Y.-Z., Tang, S.-P., & Fan, Y.-Z. 2024b, *PhRvL*, 133, 051401, doi: [10.1103/PhysRevLett.133.051401](https://doi.org/10.1103/PhysRevLett.133.051401)
- Li, Y.-J., Wang, Y.-Z., Tang, S.-P., et al. 2022, *ApJL*, 933, L14, doi: [10.3847/2041-8213/ac78dd](https://doi.org/10.3847/2041-8213/ac78dd)
- Madau, P., & Dickinson, M. 2014, *ARA&A*, 52, 415, doi: [10.1146/annurev-astro-081811-125615](https://doi.org/10.1146/annurev-astro-081811-125615)
- Mandel, I., & de Mink, S. E. 2016, *MNRAS*, 458, 2634, doi: [10.1093/mnras/stw379](https://doi.org/10.1093/mnras/stw379)
- Mandel, I., & Farmer, A. 2022, *PhR*, 955, 1, doi: [10.1016/j.physrep.2022.01.003](https://doi.org/10.1016/j.physrep.2022.01.003)
- Mandel, I., Farr, W. M., & Gair, J. R. 2019, *MNRAS*, 486, 1086, doi: [10.1093/mnras/stz896](https://doi.org/10.1093/mnras/stz896)
- McKernan, B., Ford, K. E. S., Callister, T., et al. 2022, *MNRAS*, 514, 3886, doi: [10.1093/mnras/stac1570](https://doi.org/10.1093/mnras/stac1570)
- McKernan, B., Ford, K. E. S., Bellovary, J., et al. 2018, *ApJ*, 866, 66, doi: [10.3847/1538-4357/aadae5](https://doi.org/10.3847/1538-4357/aadae5)
- Olejak, A., Klencki, J., Xu, X.-T., et al. 2024, *A&A*, 689, A305, doi: [10.1051/0004-6361/202450480](https://doi.org/10.1051/0004-6361/202450480)
- Payne, E., Kremer, K., & Zevin, M. 2024, *ApJL*, 966, L16, doi: [10.3847/2041-8213/ad3e82](https://doi.org/10.3847/2041-8213/ad3e82)
- Pratten, G., Husa, S., García-Quirós, C., et al. 2020, *PhRvD*, 102, 064001, doi: [10.1103/PhysRevD.102.064001](https://doi.org/10.1103/PhysRevD.102.064001)
- Ray, A., Magaña Hernandez, I., Breivik, K., & Creighton, J. 2024, arXiv e-prints, arXiv:2404.03166, doi: [10.48550/arXiv.2404.03166](https://doi.org/10.48550/arXiv.2404.03166)
- Santini, A., Gerosa, D., Cotesta, R., & Berti, E. 2023, *PhRvD*, 108, 083033, doi: [10.1103/PhysRevD.108.083033](https://doi.org/10.1103/PhysRevD.108.083033)
- Talbot, C., & Golomb, J. 2023, *MNRAS*, 526, 3495, doi: [10.1093/mnras/stad2968](https://doi.org/10.1093/mnras/stad2968)
- Talbot, C., & Thrane, E. 2018, *ApJ*, 856, 173, doi: [10.3847/1538-4357/aab34c](https://doi.org/10.3847/1538-4357/aab34c)
- Tiwari, V. 2022, *ApJ*, 928, 155, doi: [10.3847/1538-4357/ac589a](https://doi.org/10.3847/1538-4357/ac589a)
- Tiwari, V., & Fairhurst, S. 2021, *ApJL*, 913, L19, doi: [10.3847/2041-8213/abfb7](https://doi.org/10.3847/2041-8213/abfb7)
- Wang, Y.-Z., Li, Y.-J., Vink, J. S., et al. 2022, *ApJL*, 941, L39, doi: [10.3847/2041-8213/aca89f](https://doi.org/10.3847/2041-8213/aca89f)
- Williams, M. J., Veitch, J., Chapman-Bird, C., & Tenorio, R. 2025, *mj-will/nessai: v0.14.0.post0, v0.14.0.post0*, Zenodo, doi: [10.5281/zenodo.14627250](https://doi.org/10.5281/zenodo.14627250)
- Yang, Y., Bartos, I., Gayathri, V., et al. 2019, *PhRvL*, 123, 181101, doi: [10.1103/PhysRevLett.123.181101](https://doi.org/10.1103/PhysRevLett.123.181101)
- Zevin, M., & Holz, D. E. 2022, *ApJL*, 935, L20, doi: [10.3847/2041-8213/ac853d](https://doi.org/10.3847/2041-8213/ac853d)
- Zevin, M., Bavera, S. S., Berry, C. P. L., et al. 2021, *ApJ*, 910, 152, doi: [10.3847/1538-4357/abe40e](https://doi.org/10.3847/1538-4357/abe40e)